

Accurate modeling and positioning of a magnetically controlled catheter tip

Vi N. T. Le, Nghia H. Nguyen, and Kamal Alameh

Electron Science Research Institute, Edith Cowan University, Joondalup, WA 6027, Australia

Rukshen Weerasooriya and Peter Pratten

Point Place Ltd., Mosman Park, WA 6012, Australia

(Received 13 July 2015; revised 17 December 2015; accepted for publication 18 December 2015;
published 13 January 2016)

Purpose: This paper represents the initial phase of a proposed operator-friendly semiautomatic method for positioning and directing an intravascular three-magnet tip catheter in the human heart using an electromagnetic system.

Methods: A predictive computer algorithm based on a comprehensive mathematical model is developed, which accurately calculates the magnetic field generated by the electromagnet system as well as the magnetic torques and forces exerted on a three-magnet tip catheter, and generates the necessary electromagnet currents for arbitrary displacement and deflection of the catheter tip within a workspace of $128 \times 128 \times 128$ mm.

Results: We demonstrate the ability of the developed mathematical model to accurately position a three-magnet tip catheter within the $128 \times 128 \times 128$ mm workspace of a 3D eight-electromagnet system.

Conclusions: The ability of the developed mathematical model in predicting the displacement, direction, and deflection of the catheter tip as a function of the electromagnet current values has been verified through experimental results. © 2016 American Association of Physicists in Medicine. [http://dx.doi.org/10.1118/1.4939228]

Key words: force, torque, magnetic navigation, electromagnet, minimally invasive technique, atrial fibrillation

1. INTRODUCTION

Cardiovascular disease is one of the leading causes of mortality in the world. Half of the cardiovascular mortality is due to heart failure, i.e., progressive alteration of cardiac contraction. Cardiac contraction is entirely dependent on prior electrical activation, and therefore, a substantial number of cases of heart failure are secondary to or aggravated by electrical dysfunctions [ventricular dys-synchrony in more than 50%, atrial fibrillation (AF) in approximately 24%]. AF, in particular, diminishes the ability for the heart to function as a twin two stage pump to the body, thus reducing the fitness and capacity of the affected individual to perform daily routine duties and work. It also substantially increases the incidence of stroke, heart failure, and overall mortality.^{1–3}

AF typically develops with increasing age: Approximately 5%–10% of the population older than 60 years have this condition. Medical treatment (cardiac drugs) can diminish symptoms but does not permanently prevent the recurrence of arrhythmia. AF is a rapidly growing social, medical, and public health problem requiring a significant effort in experimental, translational, and clinical research to obtain better preventive and curative therapies and reduce the disease burden. As less than 5% of eligible patients can be currently treated by interventional ablation techniques, the number of clinical catheter laboratories dedicated to cardiac electrical disturbances is expected to be multiplied by 5 times in the next 10 years.³

One of the effective minimally invasive AF treatments is based on the use of a radio frequency (RF) catheter that ablates specific areas of the atrial myocardium in order to electrically isolate the four pulmonary veins in the left atrium.^{4,5} RF-based AF ablation procedures are significantly more effective than antiarrhythmic drugs and are performed with the aim of improving patient quality of life and reducing healthcare resource utilization in the longer term.^{6–8} Also, AF procedures help to enhance the effectiveness of standard therapeutics and ease the symptom burden for patients.⁹ However, a major time consuming technical difficulty in RF catheter procedures is to accurately manipulate the tip of the catheter into its desired position and hold it there. This requires significant training and operator dexterity, which is highly variable in clinical practice. Rapid and accurate catheter tip positioning would much improve the procedure with potential benefits in safety and efficacy as well rendering the procedure more globally applicable and predictable. Remote magnetic catheter navigation is probably also applicable to similar intraluminal procedures in other fields of medicine such as interventional radiology and vascular surgery.

Two types of magnetic catheter positioning systems have been developed, namely, the Niobe system and the catheter guidance control and imaging system (CGCI).

The Niobe system, developed by Stereotaxis Inc., St. Louis, Missouri, USA in 2004,¹⁰ produces a uniform magnetic field (of intensity 0.08 T) using two large rotating permanent magnets located on each side of the patients' torso and

mounted on robotic arms to maneuver the catheter tip inside the heart.^{11,12} However, the Niobe system has a number of drawbacks, namely, (i) it is bulky, due to the large size of the two permanent magnets, (ii) it cannot generate a high magnetic field, and (iii) it has a slow response, making it unattractive for real-time AF operations.¹³

The CGCI system, developed by Magnetecs Inc., has mainly been devised to overcome the shortcomings of the Niobe system. It comprises eight powerful coil-core electromagnets that can be placed around the torso to generate a high magnetic field (up to 0.14 T).¹⁴ Due to the spherical arrangement of its eight electromagnets, the CGCI system dynamically creates an isotropic magnetic field and gradient distribution along arbitrary directions, enabling faster motion of the catheter tip in real-time, and making it more stable.^{13,15–17} While a mathematical model for positioning the catheter in the CGCI system has been reported in Refs. 14, 17, and 18, this mathematical model is limited to single-magnet-tip catheters. Therefore, the CGCI system has not developed a mathematical model for multiseed-magnet catheters to predict their positions and make the AF ablation procedure less flexible and effective. In order to move and place any object within a magnetic field in a 3D space, the three co-ordinates X , Y , Z (at 90° to each other) must all be addressed simultaneously. In order to do this and also to allow the catheter tip to bend on itself (simulating the movement is currently possible with a tension wire catheter), the catheter needs to have magnets embedded in it responsive to variations in the field in each of these three planes. Hence, there are three embedded “seed” magnets in the respective X , Y , Z planes at the catheter tip. The reason for using a three-magnet-seed catheter is to eliminate the need for a super-elastic pull wire that steers the catheter tip. Such pull-wire is typically sheathed in a flexible compression coil that enables the catheter tip to be guided. Using a three-magnet-seed catheter will accomplish this flexibility with less force and high precision.

During the operation of these systems, the major drawbacks appear to have been related to slow speed of catheter movement, and significant loss of ability to access the patient if an emergency should occur during the procedure due to the bulky nature of the apparatus. As a result, some attempts to

accomplish this appear to have been abandoned. In addition, there have been some techniques using magnetic resonance imaging (MRI) to support for remote-controlled catheter tips in Refs. 19–21. Also, note that, inherently, MRI is not compatible with the currently proposed system, which seeks to control and perform intracardiac cavity mapping, planning, and execution of ablation using software control in a far lower intensity magnetic field (0.15 T) than is used for MR imaging.

In this paper, we present a comprehensive mathematical model that predicts the motion of a three-magnet tip catheter controlled by an externally applied magnetic field generated by an eight-electromagnet system. This model accurately predicts the position and deflection of the three-magnet tip catheter in the external magnetic field within a 3D workspace. Specifically, the model (i) calculates the torques and forces exerted on the three seed magnets embedded into the catheter tip, (ii) predicts the displacement and curvature of the catheter tip, and (iii) enables guiding the catheter tip to a desired position and along an arbitrary trajectory coupled with proof-of-concept experiments, which validate the simulation results predicted by the mathematical model.

2. SYSTEM DESCRIPTION AND MODELING

2.A. System description

The variable field eight electromagnet apparatus surrounding 250 mm spherical air space shown in Fig. 1(a) was developed in collaboration with PointPlace Ltd-Australia, and Hunan Forever Elegance Technology, China. The eight electromagnets are placed in 3D at 90° angles with respect to one another. It was designed to generate a magnetic field at a minimum of 0.15 T within a central volume of 128 × 128 × 128 mm by controlling the eight electric currents flowing through the coils of the electromagnets. The electromagnets comprised extendable cylindrical soft magnetic cores that concentrate and enhance the magnetic field strength and gradients along their centers, thus enabling fast catheter tip navigation within the central 3D workspace. Particularly, the soft magnetic material was chosen because of its ability to (i) easily magnetize with the application of an external magnetic field

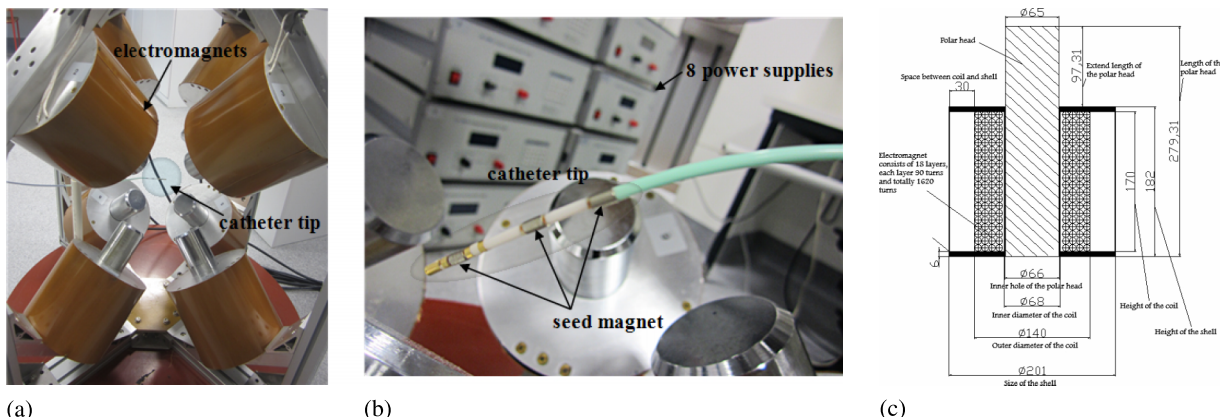


Fig. 1. (a) Photograph of the developed magnetic catheter tip positioning electromagnet system demonstrator. (b) Illustration of the catheter tip and its three seed magnets. (c) Structure of each electromagnet showing the dimensions of its components.

and quickly demagnetize as soon as the electromagnet currents are switched off. The magnetic field (up to 0.15 T) generated by the eight electromagnets was sufficient to exert the necessary torques and forces on the magnetic-tipped catheter in order to accurately position the tip to a desired target.

A 1/2 sized proof-of-concept demonstrator, having an opening sphere diameter of 25 cm and a central workspace of $128 \times 128 \times 128$ mm within which the magnetic field magnitude can be as high as 0.15 T, has been initially used for developmental and experimental purposes on the basis of cost, magnet size, energy use, and mass, prior to development of a large-scale prototype. This would require an electromagnet size increased geometrically in mass and power consumption and would still only control a similar virtual workspace (of $128 \times 128 \times 128$ mm) in the centre of the electromagnet system.

The catheter used in the experiments had three tiny permanent magnets embedded in XYZ planes, which are commercially available from several cardiac catheter producers, as illustrated in Fig. 1(b).²² The accuracy and efficiency of this three-magnet-tip catheter in positioning the catheter at desired targets has been demonstrated by Armacost *et al.*,²³ and its ability to perform tissue ablation with a higher success rate, in comparison with a single-magnet-tip, has been demonstrated by Chun *et al.*⁵ Note that a three-magnet catheter tip offers unique advantages in comparison with a single-magnet catheter tip, namely, (i) the ability to generate a higher deflection force, thus enabling the tip to reach difficult positions within the heart and (ii) the ability to rapidly change the orientation of the outer magnets, thus resulting in better alignment of the mapping catheter.⁵

It is important to note that the permanent magnets of the catheter should appropriately be spaced in order to optimize the flexibility of the catheter tip.⁷ Tension-wire-controlled catheters are currently the established norm. These have relatively rigid bodies but the final few centimeter at the tip are quite flexible. The standard size of operative intracardiac catheters introduced via the right femoral vein is 7 French. This is less than 2.33 mm in diameter. Catheters with three tiny embedded XYZ planar fixed magnets of this size with adequate flexibility that allow the tip to turn 180° on itself have already been produced commercially.

Each electromagnet has a coil (18 layers, 90 turns per layer, 1.8 mm wire diameter, and $4.10 \pm 0.05 \Omega$ resistance) and a core (made of DT4E pure iron) and is mounted on a hard aluminum frame after being accurately aligned with respect to the other electromagnets. Each electromagnet coil has an inner diameter $d_{\text{inner}} = 68$ mm, an outer diameter $d_{\text{outer}} = 140$ mm, and a length $L_{\text{coil}} = 170$ mm and is completely filled with an extractable core made of DT4E pure iron of diameter $d_{\text{core}} = 66$ mm and length $L_{\text{core}} = 279.31$ mm. The structure of each electromagnet and the dimensions of its components are shown in Fig. 1(c). In order to increase the magnetic field strength in the central workspace, cylindrical iron cores are used, which produce a magnetic field approximately 20 times stronger than the magnetic field generated by air-core-based electromagnets.¹⁵

Eight computer-controlled DC power supplies have been specifically developed to accurately and predictably vary the magnetic field, throughout the central 3D workspace. These

power supplies are controlled directly through a power supply board that converts AC input of $240\text{ V} \pm 20\text{ V}/10\text{ A}$, 50 Hz, into a DC output of $\pm 50\text{ V}/10\text{ A}$. The entire system is controlled through C# programming by a computer running under Windows 7.0 operating system and a RS232 control interface.

2.B. System modeling

2.B.1. Total magnetic field calculation

As described in Sec. 2.A, each electromagnet consists of the coil and the extractable iron cores. Consequently, the total magnetic field generated from electromagnets is computed by the summation of the magnetic field of coils and cores. In Sub-section A.1 of the Appendix, the magnetic field of the current loop is evaluated. In this paper, the analysis and calculation of the total magnetic field generated by the eight-electromagnet system are based on the Biot–Savart law.²⁴ Particularly, the mathematical model calculates the total magnetic field of eight coils and cores at any given point P in the central 3D workspace. The total magnetic field generated by a coil is first calculated at a point $P(x_P, y_P, z_P)$ by considering a current element of length dl at a point $C(x_C, y_C, z_C)$ along the coil, as illustrated in Fig. 12. The coordinates of C , $\vec{r}(C\vec{P})$, and dl can be written as

$$(x_C, y_C, z_C)_{(R_i, z_j, \theta_k)} = (R_i \cos(\theta_k), R_i \sin(\theta_k), z_j), \\ \vec{r}_{(R_i, z_j, \theta_k)} = (x_P - R_i \cos(\theta_k), y_P - R_i \sin(\theta_k), z_P - z_j), \\ \vec{dl}_{(R_i, \theta_k)} = \left(L_i \cos\left(\theta_k + \frac{\pi}{2}\right), L_i \sin\left(\theta_k + \frac{\pi}{2}\right), 0 \right),$$

with

$$L_i = \frac{2\pi R_i}{Ns}, \quad (1)$$

where R and z denote the radius of the current loop and the width of each coil turn, respectively, L is the length of each divided current element, i , j , and k are the increments for the number of layers, turns, and current elements, respectively. Using Eq. (1) and the principle of superposition, discussed earlier, the total magnetic field produced by the n th coil is expressed as follows:

$$\vec{B}_{\text{Coil } n} = \frac{\mu_0 I}{4\pi} \sum_{i=1}^{Nl} \sum_{j=1}^{Nt} \sum_{k=1}^{Ns} \frac{\vec{dl}_{(R_i, \theta_k)} \times \vec{r}_{(R_i, z_j, \theta_k)}}{r_{(R_i, z_j, \theta_k)}^3}, \quad (2)$$

where Nl , Nt , and Ns are the number of layers, turns, and current elements dl , respectively.

In order to accurately evaluate the magnetic field, the iron cores were mathematically partitioned into small magnetic dipole elements, each of volume dV and a magnetic moment dm , as shown in Fig. 2(a).^{25,26} Each soft magnetic core was considered as a continuous distribution of magnetic dipoles, each dipole having a dipole moment of $d\vec{m} = \vec{M}dV$, where M is the magnetization vector of the iron core at the magnetic dipole.

MATLAB® was used to compute the external field of each core with the input variables being the number of rounds in the vertical direction (dr is the spacing between turns), the mesh sizes along the horizontal direction (dz), and angular direction ($d\theta$). Additionally, the magnetic field and gradient produced

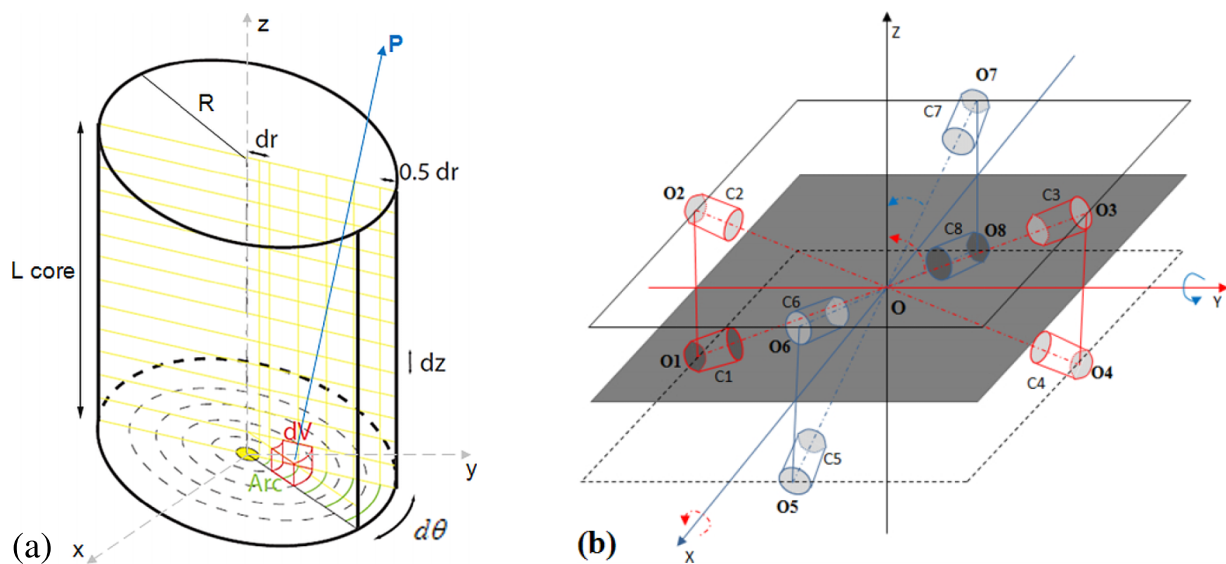


Fig. 2. (a) Diagram showing the partitioning of the iron core of an electromagnet for calculating the external magnetic field at a point P . (b) Electromagnet arrangement in 3D.

at any point P within the workspace is the summation of the magnetic fields generated by the individual point-dipoles of volume dV .^{15,27} Generally, the total magnetic field of the entire core is calculated as follows:

$$\vec{B}_{\text{core}}(\vec{m}, \vec{P}) = \frac{\mu_0 M}{4\pi} \sum_{i=1}^{Ndz} \sum_{j=1}^{Ndr} \sum_{k=1}^{Nd\theta} \frac{3 \vec{P}_{ijk} (\vec{P}_{ijk} \cdot \vec{m}_c) - \vec{m}_c}{\|\vec{P}_{ijk}\|} dV_{ijk}, \quad (3)$$

where μ_0 is the vacuum magnetic susceptibility, \vec{m}_c (A m^2) is unitary magnetic moment vector of iron core element, \vec{P}_{ijk} denotes the distance vector from the iron core elements to the point P , and dV_{ijk} is the volume of core elements.

Since all electromagnets have similar soft-magnetic cores of negligible hysteresis, the magnetic field generated by an electromagnet is linearly proportional to the electric currents driving this electromagnet, and the superposition principle can be applied to the magnetic field and the magnetic field gradient at a point P within the workspace. Accordingly, the total magnetic field at any point P is given by^{15,27,28}

$$\vec{B}(\vec{P}) = \sum_{e=1}^n \vec{B}_e(\vec{P}) = \sum_{e=1}^n \tilde{\vec{B}}_e(\vec{P}) i_e = B(\vec{P}) I, \quad (4)$$

where $e = 1, 2, \dots, n$ denotes the e th electromagnet, i_{en} is the current flowing through the e th electromagnet, $\tilde{\vec{B}}_e(\vec{P})$ is the unitary field vector, $B(\vec{P}) = [\vec{B}_1(\vec{P}) \dots \vec{B}_n(\vec{P})]$ is a $3 \times n$ field matrix at any point P and $I = [i_1 \dots i_n]^T$.

Note that, according to Ref. 29 to simplify and accelerate the computation of the total magnetic field generated by the eight electromagnets, the following homogeneous transformation matrices can be used to transform the local coordinates of each electromagnet, L^{Cn} , to the global coordinate system, L^O ,

$$L^O = R_{Cn}^O * T_{Cn}^O * L^{Cn}, \quad (5)$$

where the local coordinate systems of the eight electromagnets are translated and rotated relative to the global coordinate system $Oxyz$ through T_{Cn}^O and R_{Cn}^O .

2.B.2. Torque and force acting on the magnetically tipped catheter

Figure 3 illustrates the magnetic interaction forces exerted on the permanent magnets attached to the distal tip of the magnetic catheter. The forces between two magnetic dipoles are analyzed in the Appendix.^{30,31} In this section, we develop the analytical model for the magnetic interaction among the three permanent magnets, the position, and deflection of the catheter tip. It is important to note that the permanent magnetic seeds inserted into the long flexible tube of catheter are stiff, so they cannot be bent. Consequently, the push and pull force components \vec{F}_{pp12} and \vec{F}_{pp21} parallel to \vec{r} are equal but have opposite directions, whereas the force components \vec{F}_{pe12} perpendicular to \vec{r} exert on the catheter tip a bending moment, M_{12} , as illustrated in Fig. 3.³¹ Let (a, b) denote the angle between two vectors, \vec{a} and \vec{b} . The length of the rubber tube between two magnetic seeds is typically small, thus, it is accurate to assume that the angle between \vec{r} and \vec{m} is approximately zero. Using Subsection A.3 of the Appendix, Eq. (A4) can be rewritten as

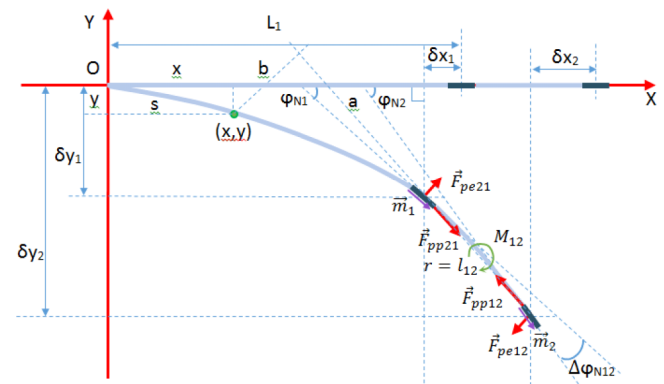


Fig. 3. Magnetic forces exerted on two seed magnets attached to the distal tip of the magnetic catheter.

$$\begin{aligned}\vec{F}_{pe12} &= \frac{3\mu_0}{4\pi r^4} ((m_1 \cos(\widehat{m_1, r}) \cdot m_2 \sin(\widehat{m_2, r})) \\ &\quad - (m_2 \cos(\widehat{m_2, r}) \cdot m_1 \sin(\widehat{m_1, r}))) \\ &= \frac{3\mu_0 m_1 m_2}{4\pi r^4} \sin(\widehat{m_2, r}).\end{aligned}\quad (6)$$

As seen from Fig. 3, the magnetic interaction between two seed magnets induces a bending moment M_{12} given by

$$M_{12}(s) = F_{pp21}b - F_{pp12}b - F_{pe21}a + F_{pe12}(l_{12} + a). \quad (7)$$

Thus,

$$M_{12}(s) = F_{pe}l_{12} \text{ since } F_{pe21} = F_{pe12} = F_{pe}, \quad F_{pp21} = F_{pp12}. \quad (8)$$

Using Eqs. (A4) and (8), for a three-permanent-magnet embedded catheter, the bending moments exerted on the magnet seeds are

$$M_{12} = \frac{3\mu_0 m^2}{4\pi l_{12}^3} \sin(\Delta\varphi_{N12}) \text{ with } \Delta\varphi_{N12} = \varphi_{N1} - \varphi_{N2}, \quad (9)$$

$$M_{23} = \frac{3\mu_0 m^2}{4\pi l_{23}^3} \sin(\Delta\varphi_{N23}) \text{ with } \Delta\varphi_{N23} = \varphi_{N2} - \varphi_{N3}, \quad (10)$$

$$M_{13} = \frac{3\mu_0 m^2}{4\pi l_{13}^3} \sin(\Delta\varphi_{N13}) \text{ with } \Delta\varphi_{N13} = \varphi_{N1} - \varphi_{N3}, \quad (11)$$

where φ_{Nm} , $m = 1, 2, 3$ is the angle between the x -axis and the dipole moment vector of m th magnetic seed. Note that the bending moments depend on the angles $\Delta\varphi_{N12}$, $\Delta\varphi_{N23}$, $\Delta\varphi_{N13}$

and the separation distances l_{12} , l_{23} , l_{13} , between the magnetic seeds.

The dimensions of the catheter tip used in this mathematical model were taken from the specifications of the irrigated gold tip catheter Trignum Flux G, made by Biotronik, Germany. This catheter was particularly adopted because of its flexibility, safe operation, and ablation effectiveness.^{13,32} Each of the three identical cylindrical permanent seed magnets has a length of 6-mm and a diameter of 2.3 mm, and the spacing between the first and second seed magnets and the second and third seed magnets is 9.5 and 15.5 mm, respectively, as illustrated in Fig. 4(a). The magnetic seeds are made using an alloy of neodymium-iron-boron (NdFeB), which exhibits a remanent magnetization of approximately 5×10^5 A/m.^{16,33,34} Particularly, this ferromagnetic material is widely utilized in catheter designs, because it has a strong magnetization, making it an excellent candidate for steering catheter tips.^{35–37} The finite element method was applied for the simulation of the curvature of the catheter tip under an external magnetic field, taking into account the magnetic interaction among seed magnets. Note that, in this paper, we concentrate on analyzing the torques and forces exerted on the three magnetic seeds; other factors such as the four electrodes embedded into the catheter tip were neglected, because they have negligible impact on the catheter motion.³⁸

As discussed in the Appendix, the Euler–Bernoulli beam theory was applied to establish the equilibrium equation of

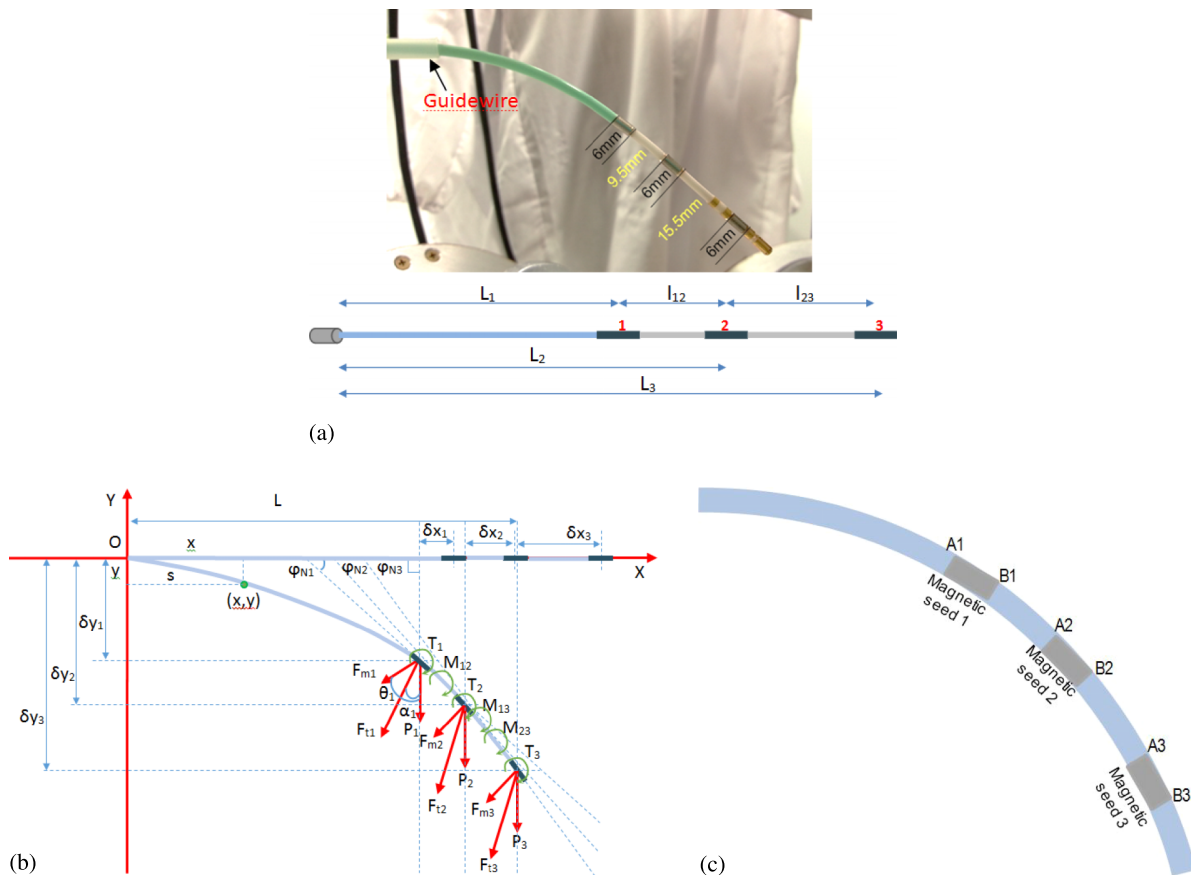


Fig. 4. (a) Irrigated gold tip catheter and its dimensions. (b) Illustration of the distribution of forces, bending moments, and torques exerted on the three seed magnets of the catheter. (c) Definition of points $\{A_i, B_i\}$ on the magnet seeds.

the catheter tip in an external magnetic field. Obviously, some parameters needed to be defined, such as the slope at any point $C(x, y)$ with respect to the x -axis, φ , and the arc length from the fixed end of the catheter tip to point $C(x, y)$, s . Furthermore, the bending rigidity of the catheter tip was modeled through two different values, namely, the lengths L_1 , l_{12} , and l_{23} , illustrated in Fig. 4(a). Next, Fig. 4(b) illustrates the forces, bending moments, and torques typically exerted on the three seed magnets of the catheter. The total forces $\{F_{t1}, F_{t2}, F_{t3}\}$ exerted on three magnets are the sums of the magnetic forces $\{F_{m1}, F_{m2}, F_{m3}\}$ and gravitational forces $\{P_1, P_2, P_3\}$. In order to determine the catheter position, it is necessary to evaluate the horizontal and vertical displacements, $\{\delta_{x1}, \delta_{x2}, \delta_{x3}\}$ and $\{\delta_{y1}, \delta_{y2}, \delta_{y3}\}$, as well as the angles $\{\varphi_{N1}, \varphi_{N2}, \varphi_{N3}\}$. Note that we assume that the seed magnets inserted into the long flexible tube of catheter are stiff, so they cannot be bent as illustrated in Fig. 4(c).

Being made of permanent magnetic materials, the magnetization M of each magnet seed is independent of the magnetic field generated by the electromagnet system. Furthermore, the magnetization of each magnetic seed depends on the remanent magnetization of NdFeB and shape of the seed. The torque exerted on a magnet seed depends on the angle between \vec{M} and \vec{B} , which can be adjusted incrementally up to 90° . To increase the force exerted on a permanent magnet seed, the magnetic gradient must be increased through the control of the distribution of the magnetic field generated by the electromagnet system.²⁸ Note that in order to accurately model the catheter motion, it is important to take into account not only the magnetic torques induced by the cross products of the applied magnetic field and magnetic moments but also the torques generated by the cross products of the lever-arm distance and the total forces (including magnetic forces and gravitational forces).

2.B.3. Catheter equilibrium state modeling

As mentioned earlier, the catheter is inextensible and has a long thin body with a diameter that is much smaller than its length, as illustrated in Fig. 4. Therefore, the Euler–Bernoulli beam model can be applied to predict the curvature of the catheter.^{38–42} Besides, the catheter can be considered as a cantilever beam that is fixed at one end and is free at the other end. According to the study of the deflection of the cantilever beam reported by Feynman, Leighton, and Sands,⁴⁰ the Euler–Bernoulli bending moment (M)-curvature (φ) relationship can be expressed as $EI d\varphi/ds = M$, where $d\varphi/ds$ is the curvature of the catheter at any point along its length, M denotes the bending moment, and EI is bending rigidity of the catheter. By differentiating

this equation with respect to s , we obtain⁴²

$$EI \frac{d^2\varphi}{ds^2} = \frac{dM}{ds}. \quad (12)$$

The total bending moment can be expressed as the sum of the bending moments acting on the three magnets of the catheter tip, that is,

$$M(s) = \begin{cases} M_1(s) + M_2(s) + M_3(s) + M_0(s), & 0 < s < L_1 \\ M_2(s) + M_3(s) + M_0(s), & L_1 < s < L_2 \\ M_3(s) + M_0(s), & L_2 < s < L_3 \end{cases} \quad (13)$$

Note that, unlike the simplified analysis presented in Ref. 42, where the deflection of the beam is caused by one vertical concentrated load at the free end, and the mass of beam is omitted, the weight of catheter tip is taken into account in the modeling. Based on Fig. 4(b), assuming that the components of the total forces $\{F_{t1}, F_{t2}, F_{t3}\}$ along the x - and y -axes are $\{F_{t1x}, F_{t2x}, F_{t3x}\}$ and $\{F_{t1y}, F_{t2y}, F_{t3y}\}$, respectively, therefore, the bending moments M_1 , M_2 , M_3 , and M_0 at the three seed magnets and the fixed end of the catheter, respectively, can be expressed as

$$M_1(s) = F_{t1y}(L_1 - \delta_{x1} - x) + F_{t1x}(\delta_{y1} - y), \quad (14)$$

$$M_2(s) = F_{t2y}(L_2 - \delta_{x2} - x) + F_{t2x}(\delta_{y2} - y), \quad (15)$$

$$M_3(s) = F_{t3y}(L_3 - \delta_{x3} - x) + F_{t3x}(\delta_{y3} - y), \quad (16)$$

$$M_0 = \begin{cases} T_1 + T_2 + T_3 + M_{12} + M_{23}, & 0 < s < L_1 \\ T_2 + T_3 + M_{23}, & L_1 \leq s < L_2 \\ T_3, & L_2 \leq s < L_3 \end{cases} \quad (17)$$

Equation (17) shows that a moment M_0 applied at the end of the tip is the total of magnetic torques T_1 , T_2 , T_3 produced by the external magnetic field and the bending moments M_{12} , M_{23} , M_{13} among three magnets. It is essential to note that the spacing between the seed magnets is intentionally made different in order to make the magnetic interaction between them negligible.³¹

Differentiating from Eqs. (14) to (17) with respect to s , and using $dM_0/ds = 0$ (because the components of the bending moment M_0 are independent of the distance s), $dx/ds = \cos \varphi$, and $dy/ds = \sin \varphi$, the equilibrium equation for the catheter tip can be expressed as follows.^{42,43}

$$EI \frac{d^2\varphi}{ds^2} + F_{t1y} \cos \varphi_n + F_{t1x} \sin \varphi_n + F_{t2y} \cos \varphi_n + F_{t2x} \sin \varphi_n + F_{t3y} \cos \varphi_n + F_{t3x} \sin \varphi_n = 0. \quad (18)$$

The boundary conditions for this differential equation are

$$\varphi|_{s=0} = 0; \quad \left. \frac{d\varphi_n}{ds} \right|_{s=0} = 0, \quad (19)$$

$$\frac{d\varphi_{N1}}{ds} = \frac{l_{12}F_{t2y} \cos \varphi_N + l_{12}F_{t2x} \sin \varphi_N + l_{13}F_{t3y} \cos \varphi_N + l_{13}F_{t3x} \sin \varphi_N + M_0}{EI}, \quad (20)$$

$$\frac{d\varphi_{N2}}{ds} = \frac{l_{23}F_{t3y} \cos \varphi_{(N1)} + l_{23}F_{t3x} \sin \varphi_{(N1)} + M_0}{EI}, \quad (21)$$

$$\frac{d\varphi_{N3}}{ds} = \frac{M_0}{EI}, \quad (22)$$

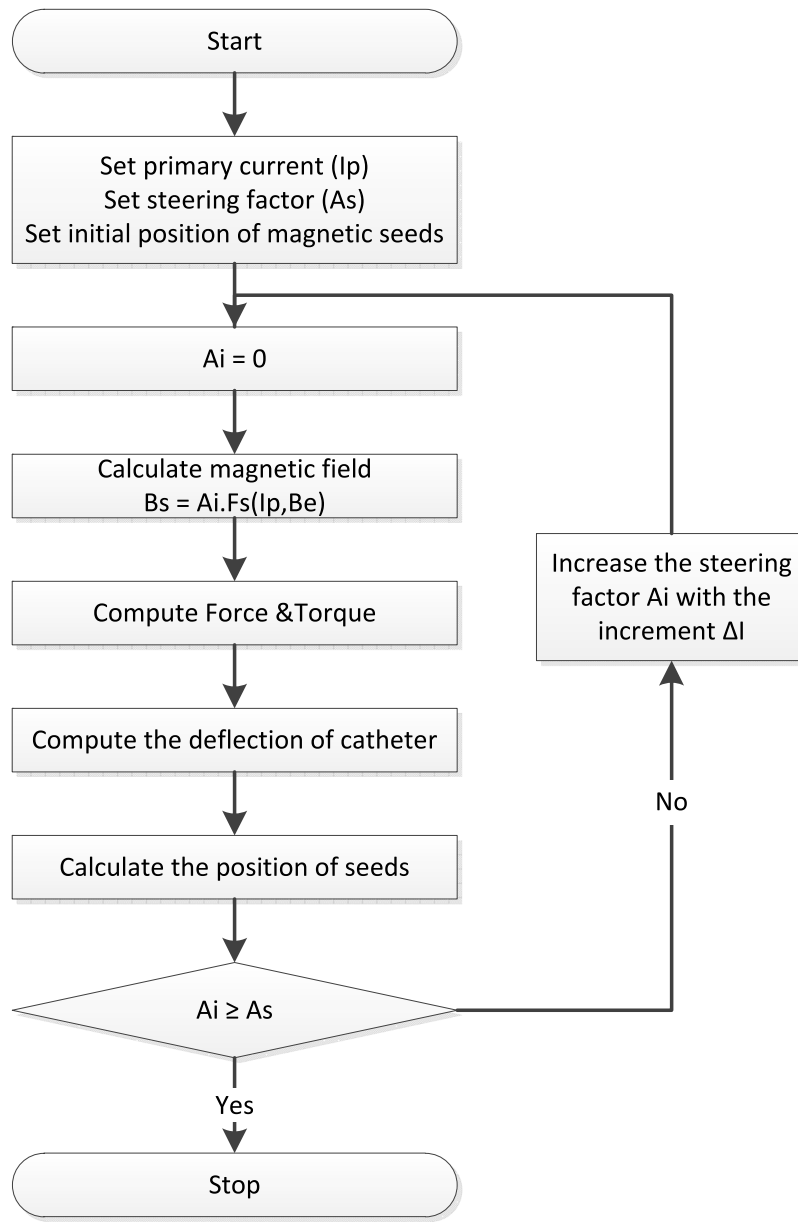


FIG. 5. A flowchart illustrating the iterative algorithm used to find a new equilibrium position of the catheter tip in the workspace.

where $d\varphi_n \triangleq \varphi_n - \varphi_{(n-1)}$. In addition, assume that $\{A_i, B_i\}$ are the points at the front end of the i th permanent magnet seed, as shown in Fig. 4(c), since the three seed magnets are not flexible materials, they cannot be deformed like the elastic material of the catheter body. In other words, for points within the three seed magnets, the bending constraints of seed magnets are expressed as follows:

$$\varphi|_{s \in [A_i, B_i]} = \text{constant}. \quad (23)$$

The relaxation method is typically used for boundary value problems.⁴⁴ However, this method is inherently time consuming and results in relatively high errors when implemented using MATLAB software, making it impractical for real-time catheter positioning. To solve Eq. (18) with the above initial and boundary conditions, “MATLAB bvp4c solver” is adopted. This method starts with an initial guess supplied at an initial mesh of points and divides the interval of integration into

subintervals, then, the error is estimated at each subinterval and the mesh size is dynamically changed until the specified accuracy is attained.⁴⁵⁻⁴⁷

2.B.4. Magnetic catheter guidance model

The guidance of the magnetic catheter is typically realized by generating the appropriate external magnetic field that produces the moments necessary for bending the catheter to a desired angle. For the electromagnet system demonstrator shown in Fig. 1(a), the external magnetic field is generated by driving the electromagnets with a set of electric currents, called driving current matrix \bar{I} . The magnetic field, forces, and torques exerted on the magnet seeds can be calculated using Eqs. (4), (A2), and (A3). The magnetic forces and torques, which depend on the spacing, shape, and size of the magnetic seeds, induce bending moments that can be calculated using

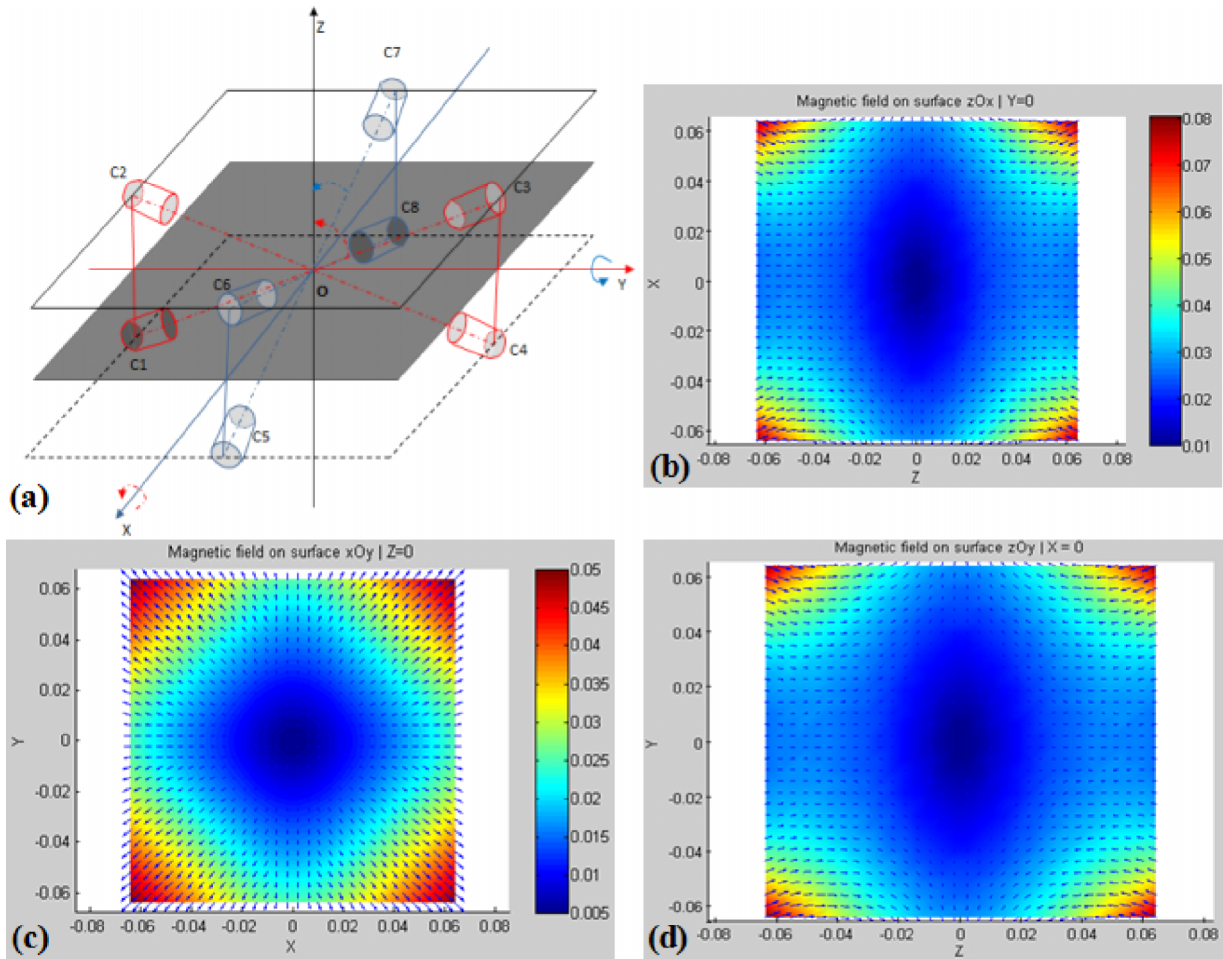


FIG. 6. (a) Electromagnets and the reference plane xOy (in gray color). (b)–(d) Simulated distribution of the total magnetic field generated by the eight electromagnets (driven by equal currents) in planes xOy , yOz , and xOz , respectively.

Eq. (12). While the catheter tip and permanent magnet seeds can be moved while the catheter is bending, it is typically difficult to directly determine the position of the catheter for a given driving current matrix \bar{I} , because the magnetic force and torque exerted on the catheter's magnet seeds are not constant when the catheter is being deflected. Because of this issue, an iterative algorithm was especially developed, which executes steps in iterations and successive approximations in order to obtain the catheter's position.

The algorithm can be described as follows: The calculation begins with the initial position of the magnetic seeds, then, the magnetic forces and torques are computed according to the current position of catheter tip, and then, the various bending moments are obtained to predict the new position of the catheter. The calculation of the forces and torques is then repeated with the new position and the process is iterated until the predicted position of catheter tip converges to the stable position that satisfies the boundary conditions. Note that if the distance between the consecutive catheter positions as well as the difference between the consecutive values of the forces and torques are large, convergence may not be practically attainable. To solve this issue, we propose a fast and efficient calculation method that can be described as follows:

First, instead of conventionally recalculating the magnetic field at the position of the magnetic seeds when the catheter is bent, the magnetic field distribution generated within the 3D workspace by eight electromagnets with unitary driving electric currents (I_u) is precomputed and stored as a 3D matrix $B_e = \{B_{e1}, B_{e2}, \dots, B_{e8}\}$. Then, the magnetic field distribution, B_s , around the catheter seeds (for a catheter position s) is rapidly calculated from B_e , and can be represented by a function F_s given by

$$B_s = F_s(I, B_e) \triangleq \sum_{i=1}^8 \frac{I_i}{I_u} \cdot B_{ei}(s). \quad (24)$$

Second, to accelerate the convergence of the iterations to the equilibrium position of the catheter tip, we express each driving current flowing through each electromagnet as the product of two parts, namely, a primary current, I_P , and a steering factor, A_S , that is,

$$\bar{I} = A_S \cdot I_P. \quad (25)$$

Using Eqs. (24) and (25) yields

$$B_s = A_S \cdot F_s(I_P, B_e). \quad (26)$$

The primary current matrix $I_P = [I_{P1}, I_{P2}, \dots, I_{P8}]$ affects the direction of magnetic field, while the steering factor, A_S , steers

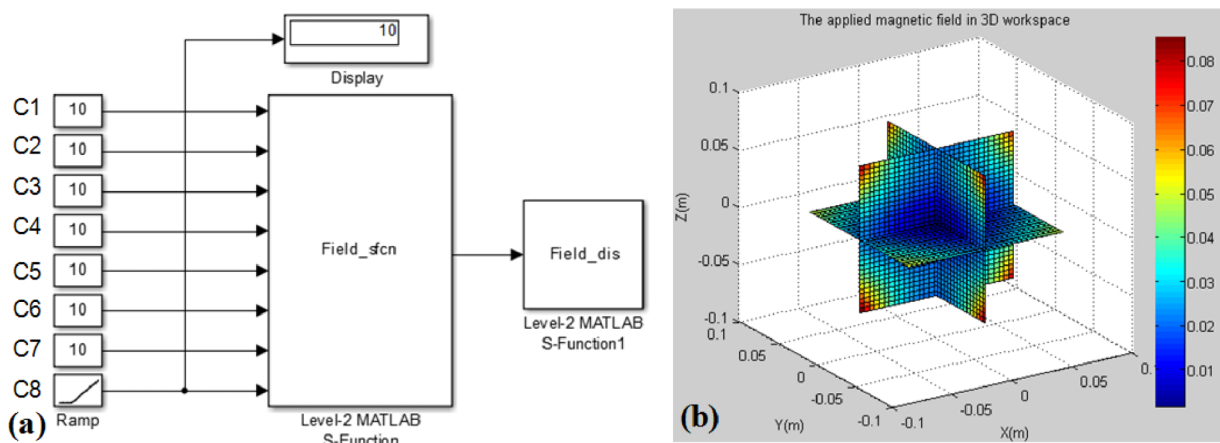


FIG. 7. (a) Simulink block diagram illustrating the simulation procedure adopted for varying the electromagnet currents and displaying the magnetic field distribution. (b) Simulated total magnetic field distribution in the 3D workspace for similar electromagnet currents.

the magnetic field direction through small current increments that gradually change the direction and magnitude of the magnetic field to the desired value.

Third, an iterative process is used to determine the equilibrium position of catheter tip, which is illustrated by the flow chart shown in Fig. 5. Particularly, the tip is first placed along a defined initial position within the central workspace with zero driving currents. Next, we gradually increase the current values of the eight electromagnets. The distribution of the generated magnetic field is then calculated at every

increment of the electric current to evaluate the forces and torques exerted on the catheter and the next stage is to compute the new position and deflection of the catheter tip at every increment of the electric current. The iterative algorithm is executed until the solution for the final equilibrium position of the catheter tip converges. Note that, by reducing the current increment, the catheter can be positioned more accurately at a desired destination; however, the convergence time increases. Therefore, a trade-off exists between the catheter positioning accuracy and algorithm convergence time. For a 2-mm spacing

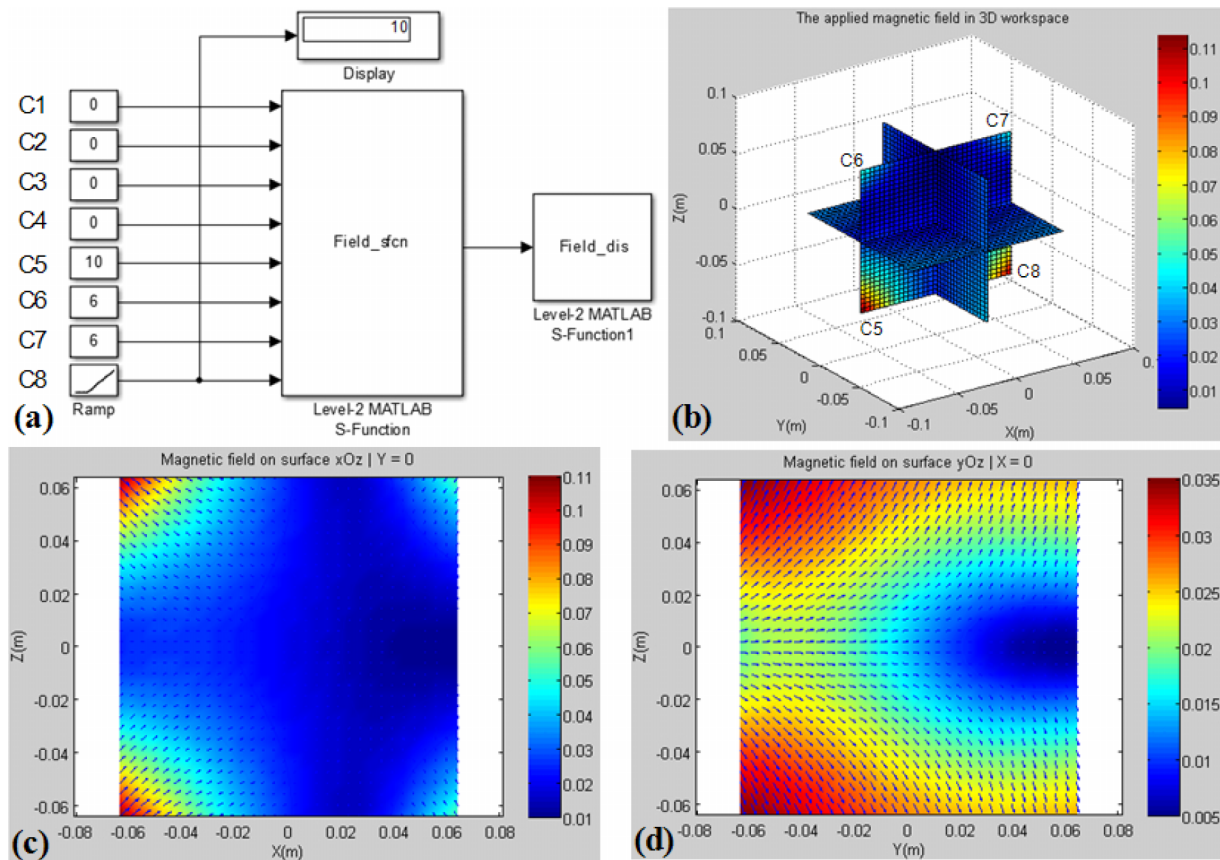


FIG. 8. (a) Simulink block diagram for electromagnet current matrix $[0\ 0\ 0\ 0\ 10\ 6\ 6\ 10]$ A. (b) Simulated total magnetic field distribution in the 3D workspace. (c) and (d) Magnetic field vector distributions in the zOx and zOy planes, respectively.

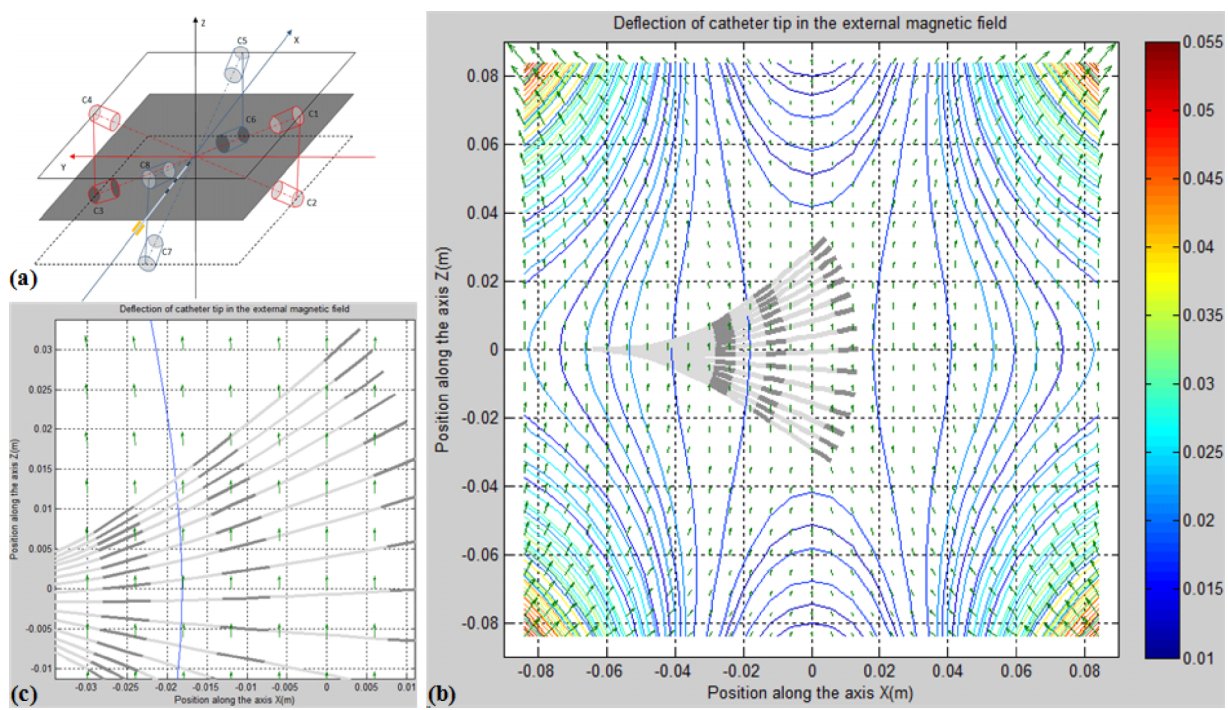


FIG. 9. (a) Illustration of the electromagnet system, (b) simulated catheter tip deflection in the applied magnetic field, and (c) zoom-in of (b).

between the initial and final positions (this represents a practical scenario in AF operations), the execution time is around 10 s. Obviously, for a larger spacing between the initial and final positions more execution time is needed.

3. RESULTS AND DISCUSSION

3.A. Simulation results

3.A.1. Simulation of the external magnetic field

For the catheter tip positioning system shown in Fig. 1(a), the distance between the ends of two opposite electromagnets is 250 mm. For simulation, the $128 \times 128 \times 128$ mm central 3D workspace is partitioned into eight regions. The mathematical model described in Sec. 2 was implemented in MATLAB. Figures 6(b)–6(d) show simulated distributions of the magnetic field in the planes xOy , yOz , and xOz , for equal electromagnet currents of 10 A. It is obvious that the magnetic field is strongest at the cores and diminishes at the centre, O , of the workspace. At distances 0, 20, 40, 60, 80, 100, and 120 mm between the centre O and the core of electromagnet 1, for example, the magnetic field strengths are 0.012, 0.017, 0.0244, 0.0366, 0.0595, 0.1003, and 0.136 T, respectively.

MATLAB's simulink package was used to investigate the perturbations in the magnetic field when the electromagnet current intensities are varied. The block diagrams shown in Figs. 7(a) and 8(a) illustrate the simulation procedure followed to vary the electromagnet currents and plot the magnetic field distributions. The simulation procedure comprises (i) *Field_sfcb* block that computes the magnetic field for a given input current value based on the mathematical model discussed above and *Field_dis* block that displays the magnetic field

distributions. Both blocks are inherently built into level-2 MATLAB's *s*-function.

In the simulation case illustrated Fig. 7(a), it was assumed that the currents driving the eight electromagnets have equal magnitudes, of 10 A. The simulated magnetic field distribution, displayed in Fig. 7(b), exhibits symmetry in planes xOy , yOz , and xOz with zero magnetic field at the central point O of the system. In this case, when the catheter tip is put into the workspace of this system, it is almost at equilibrium.

Now, let us investigate the effect of changing the electromagnet current values on the magnetic field distribution. Figure 8(a) shows the Simulink block diagram for a scenario where the electromagnet currents were changed to 0 A for electromagnets C1, C2, C3, and C4, 10 A for electromagnets C5 and C8 and 6 A for electromagnets C6 and C7. The simulated magnetic field distribution, shown in Fig. 8(b), reveals that, in this case, the magnetic field is highest around electromagnets 5 and 8. Therefore, if the catheter tip is placed in the

TABLE I. Parameters representing the properties of the magnetic seeds and catheter used in the simulation model.

| Parameter | Symbol | Value |
|---|------------------------|------------------------|
| Bending stiffness | EI ($N \cdot m^2$) | 9×10^{-6} |
| Magnetization | M (A/m) | 5×10^5 |
| Magnetic seed density | kg/m^3 | 7500 |
| Diameter of magnetic seed | r (m) | 0.0023 |
| Volume of hollow cylindrical seed | V (m^3) | 1.923×10^{-8} |
| Mass of each hollow cylindrical seed | w (kg) | 1.44×10^{-4} |
| Length between the guidewire and 1st seed | L_1 (m) | 0.040 |
| Length between the 1st and 2nd seed | L_{12} (m) | 0.015 |
| Length between the 2nd and 3rd seed | L_{23} (m) | 0.021 |

TABLE II. Magnetic torques and moment of forces for the scenario shown in Fig. 9(b).

| Magnetic torque (N m) | | | Moment of force (N m) | | |
|------------------------|------------------------|------------------------|-----------------------|-----------------------|------------------------|
| 1st seed | 2nd seed | 3rd seed | 1st seed | 2nd seed | 3rd seed |
| -8.25×10^{-6} | -7.77×10^{-6} | -7.08×10^{-6} | 1.29×10^{-6} | 1.73×10^{-6} | 1.67×10^{-6} |
| -1.70×10^{-5} | -1.60×10^{-5} | -1.48×10^{-5} | 2.76×10^{-6} | 3.06×10^{-6} | 2.95×10^{-6} |
| -2.63×10^{-5} | -2.49×10^{-5} | -2.34×10^{-5} | 4.43×10^{-6} | 4.73×10^{-6} | 9.91×10^{-7} |
| -3.58×10^{-5} | -3.34×10^{-5} | -3.26×10^{-5} | 6.20×10^{-6} | 4.13×10^{-6} | -5.88×10^{-7} |
| -4.53×10^{-5} | -4.26×10^{-5} | -4.21×10^{-5} | 7.64×10^{-6} | 5.00×10^{-6} | -2.37×10^{-6} |
| -5.47×10^{-5} | -5.16×10^{-5} | -5.12×10^{-5} | 9.30×10^{-6} | 5.41×10^{-6} | -3.74×10^{-6} |
| -6.36×10^{-5} | -6.00×10^{-5} | -5.92×10^{-5} | 1.07×10^{-5} | 6.22×10^{-6} | -4.14×10^{-6} |
| -7.20×10^{-5} | -6.74×10^{-5} | -6.60×10^{-5} | 1.20×10^{-5} | 6.91×10^{-6} | -3.28×10^{-6} |
| -7.95×10^{-5} | -7.42×10^{-5} | -7.16×10^{-5} | 1.31×10^{-5} | 8.52×10^{-6} | -1.08×10^{-6} |
| -8.65×10^{-5} | -8.02×10^{-5} | -7.68×10^{-5} | 1.39×10^{-5} | 9.24×10^{-6} | 4.20×10^{-7} |
| -9.32×10^{-5} | -8.59×10^{-5} | -8.10×10^{-5} | 1.46×10^{-5} | 9.87×10^{-6} | 4.77×10^{-6} |
| -0.000 1 | -9.36×10^{-5} | -8.61×10^{-5} | 1.63×10^{-5} | 1.64×10^{-5} | 1.21×10^{-5} |
| -0.000 11 | -9.91×10^{-5} | -8.99×10^{-5} | 1.69×10^{-5} | 1.72×10^{-5} | 1.89×10^{-5} |
| -0.000 11 | -0.0001 | -9.25×10^{-5} | 1.72×10^{-5} | 1.75×10^{-5} | 2.16×10^{-5} |

centre of the workspace, it moves upward to a new equilibrium position. Figures 8(c) and 8(d) show the magnetic field vector distributions in the zOx and zOy planes, which are useful for calculating the forces and torques exerted on the catheter tip.

3.A.2. Simulation of catheter tip deflection

In order to determine the current position of the catheter tip in the workspace, it is important to map the local coordinate system of the catheter into the global coordinate system of the eight-electromagnet system. We assume that the three-magnet tip catheter is placed along the negative direction of the x -axis in plane xOz , and that, the guidewire position is at a distance 0.064 m from the center O of the workspace, as illustrated in Fig. 9. The simulated magnetic field distributions present the progressive deflection of the catheter tip, when the electromagnet current values progressively increased from 0 to

1.7 A. Note that for all displacements, the magnetic seeds are aligned with the direction of the magnetic field, as illustrated in Fig. 9(c), which is a zoom-in of Fig. 9(b). Table I shows the parameters of the magnetic seeds and catheter used in the simulation.

Table II shows the simulated magnetic torques and moments of force exerted on the magnetic seeds [for the scenario discussed in Fig. 9(b)], which play a key role in steering the three-magnet tip catheter. When the catheter tip is further bent via a higher electric current, the magnetic torques, and moments of force exerted on three magnetic seeds also vary.

3.B. Experimental results of magnetic catheter control

The length of the catheter tip part outside the guidewire was 40 mm in Fig. 10(a), and in the experiments, the initial direction of the catheter tip was along the z -axis and the driving

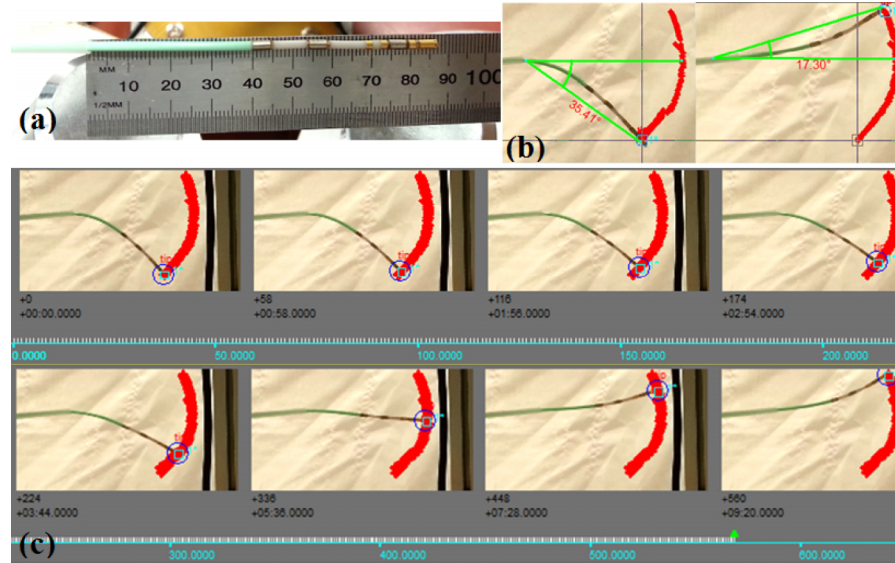


FIG. 10. (a) The 40-mm length of the catheter tip part outside the guidewire. (b) Initial and final positions of the catheter for a proof-of-concept bending scenario, and (c) measured intermediate positions of the catheter tip under an externally applied magnetic field with a set of electromagnet currents between 0 and 7 A, which correspond to the initial and final catheter positions, respectively.

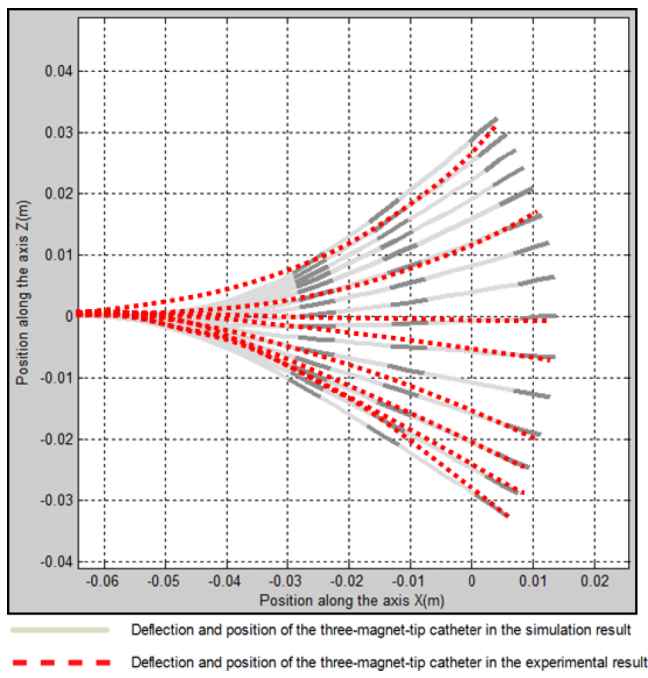


FIG. 11. Simulated and measured catheter deflection angles and positions, extracted from Figs. 9 and 10.

currents were generated through a computer algorithm, especially developed to position the catheter tip within the central workspace. Also, ProAnalyst® software was used to track the motion of the catheter tip from an initial position (zero electric currents) to a final equilibrium position (electric currents of 7 A for all electromagnets). Subsequently, ProAnalyst-based angle measurements demonstrate the ability of the electromagnet system to bend the catheter from -35.41° to $+17.30^\circ$, this corresponds to a total bending angle of 52.71° (from the initial position to the final position), as shown in Fig. 10(b). It is important to note that this bending scenario in Fig. 10(b) has been used to demonstrate the concept of the magnetically guided catheter. In fact, the bending angle can be as much as 180° . Figure 10(c) shows the progressive displacements of the catheter when the driving currents were gradually increased from 0 to 7 A. The experimental results of the catheter movement displayed in Fig. 10 demonstrate the potential of the developed mathematical model as well as the principle of catheter tip positioning system.

Figure 11 shows the simulated and measured catheter deflection angles and positions, extracted from Figs. 9 and 10. It is clear from Fig. 11 that very good agreement between the simulated and measured catheter deflection angles and positions is attained, thus demonstrating the accuracy of the developed mathematical modeling software.

Note that catheter position detection is the subject of further separate on-going work, which is beyond the scope of this paper, and will be published elsewhere.

4. CONCLUSION

A comprehensive mathematical model has been developed, which accurately positions the deflection of a three-

permanent-magnet tip catheter through an externally applied magnetic field. The magnetic field produced by the eight-electromagnet system has been accurately modeled. An analytical torque and force model taking into account the interaction between the three magnetic seeds attached into the catheter tip and the externally applied magnetic field has also been developed. In addition, we developed an iterative algorithm for use in conjunction with MATLAB's bvp4c solver to predict the equilibrium condition of the catheter tip for arbitrary electromagnet current values. Finally, the ability of the developed mathematical model in predicting the displacement, direction, and deflection of the catheter tip as a function of the electromagnet current values has been verified through experimental results.

This work seeks to demonstrate the ability to accurately control the tip of the catheter with three tiny embedded fixed magnets (seeds) near its tip, such that it can be positioned and moved within the designated virtual cube. The current experiment employs eight magnets but the translation of the mathematical simulation to any array of magnets greater than six (the minimum for X, Y, Z 3 dimensional control) is entirely possible.

It is envisioned that as work progresses, further papers will address the ability of the control to be standardized and synchronized for optimal accuracy within each particular person.

APPENDIX: THEORETICAL CALCULATION OF MAGNETIC FIELDS, MAGNETIC TORQUE AND FORCES

1. Magnetic field calculation

The eight iron-core electromagnet system shown in Fig. 1 consists of two main parts, namely, the coils and iron cores. To model the magnetic field generated by a coil, current-carrying wires are defined as current loops wrapped around the magnetic core of the coil. Each current loop is divided into current elements $d\vec{l}$, as illustrated in Fig. 12. Generally, the external magnetic field produced by each current loop at any given point P can be computed by using the Biot–Savart law and the superposition principle.^{24,33,48} Therefore, the magnetic field generated by the entire current loop can be expressed as²⁴

$$\vec{B}(P) = \frac{\mu_0 I}{4\pi} \oint \frac{d\vec{l} \times \vec{r}}{r^3}, \quad (\text{A1})$$

where \vec{r} denotes the vector directed from $d\vec{l}$ toward the point P , $r = |\vec{r}|$ is the distance from $d\vec{l}$ to P , and $\mu_0 = 4\pi \times 10^{-7} \text{ T m/A}$ is the permeability of free space.

2. Magnetic torque and force exerted on the magnetic-tipped catheter

A detailed mechanical model for a single-magnet catheter tip analyzing torques and forces has been reported by Tunay.³⁸ However, the limitation of this model is that it is limited to one-magnet tip catheters. In this paper, we present a comprehensive mathematical model capable of predicting the torques and

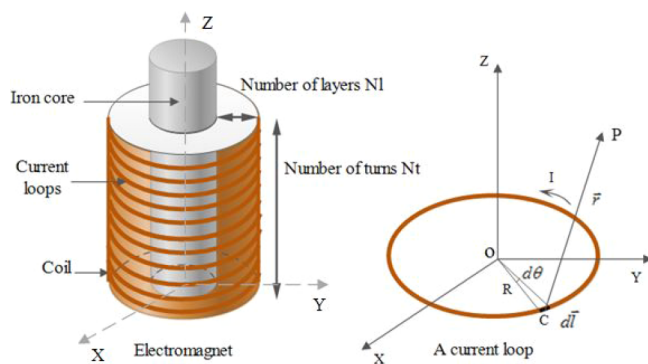


FIG. 12. Partitioning a current loop to calculate the magnetic field.

forces exerted on a three-magnet tip catheter. Basically, for a magnetic field distribution of flux density \vec{B} , the catheter tip is typically displaced and bent due to the magnetic torques (\vec{T}) and forces (\vec{F}) exerted on three magnetic seeds. Assuming that all magnetic seeds have a magnetization \vec{M} (A/m) and a volume V (m³), then, the magnetic torque and force can be expressed as^{15,38,49}

$$\vec{T} = V \cdot \vec{M} \times \vec{B}, \quad (\text{A2})$$

$$\vec{F}_m = \nabla_B (\vec{m} \cdot \vec{B}) = V \left[\frac{\partial \vec{B}}{\partial x} \quad \frac{\partial \vec{B}}{\partial y} \quad \frac{\partial \vec{B}}{\partial z} \right]^T \vec{M}, \quad (\text{A3})$$

where ∇_B is the gradient operator and \vec{m} (A m²) is the magnetic moment of each magnetic seed ($\vec{m} = V \cdot \vec{M}$). Note that the torque tends to align the permanent magnets embedded into the catheter tip with the applied magnetic field, whereas the forces (N) pull the tip along the direction of the field gradient toward a local maximum.³⁴

3. Force between two magnetic dipoles

Villani has developed a model that predicts the forces between two magnetic dipoles and validated this model via two methods, namely, using vector differentiation and path integration.³⁰ Specifically, for two magnetic dipoles of magnetic moments \vec{m}_1 and \vec{m}_2 , Villani model expresses the force exerted on the first magnetic dipole due to the second dipole moment as

$$\vec{F}_{12} = \frac{3\mu_0}{4\pi r^5} \left(\vec{m}_1 (\vec{r} \cdot \vec{m}_2) + \vec{m}_2 (\vec{r} \cdot \vec{m}_1) + \vec{r} (\vec{m}_1 \cdot \vec{m}_2) - \frac{5\vec{r}(\vec{r} \cdot \vec{m}_1)(\vec{r} \cdot \vec{m}_2)}{r^2} \right), \quad (\text{A4})$$

where $\mu_0 = 4\pi \times 10^{-7}$ T m/A is the permeability of free space, \vec{r} is the vector from the central point of the first magnet to the central point of the second magnet, and $\hat{r} = \vec{r}/|\vec{r}|$ is the unit vector parallel to \vec{r} .

¹R. Weerasooriya, P. Khairy, J. Litalien, L. Macle, M. Hocini, F. Sacher, N. Lellouche, S. Knecht, M. Wright, and I. Nault, "Catheter ablation for atrial fibrillation: Are results maintained at 5 years of follow-up?", *J. Am. Coll. Cardiol.* **57**(2), 160–166 (2011).

²C. Bonanno, M. Paccanaro, L. La Vecchia, R. Ometto, and A. Fontanelli, "Efficacy and safety of catheter ablation versus antiarrhythmic drugs for atrial fibrillation: A meta-analysis of randomized trials," *J. Cardiovasc. Med.* **11**(6), 408–418 (2010).

- ³R. Cappato, H. Calkins, S.-A. Chen, W. Davies, Y. Iesaka, J. Kalman, Y.-H. Kim, G. Klein, A. Natale, and D. Packer, "Updated worldwide survey on the methods, efficacy, and safety of catheter ablation for human atrial fibrillation," *Circ.: Arrhythmia Electrophysiol.* **3**(1), 32–38 (2010).
- ⁴O. Wazni, B. Wilkoff, and W. Saliba, "Catheter ablation for atrial fibrillation," *N. Engl. J. Med.* **365**(24), 2296–2304 (2011).
- ⁵J. K.-R. Chun, S. Ernst, S. Matthews, B. Schmidt, D. Bansch, S. Boczor, A. Ujeyl, M. Antz, F. Ouyang, and K.-H. Kuck, "Remote-controlled catheter ablation of accessory pathways: Results from the magnetic laboratory," *Eur. Heart J.* **28**(2), 190–195 (2007).
- ⁶H. Rafii-Tari, C. J. Payne, and G.-Z. Yang, "Current and emerging robot-assisted endovascular catheterization technologies: A review," *Ann. Biomed. Eng.* **42**(4), 697–715 (2014).
- ⁷Y. Fu, H. Liu, W. Huang, S. Wang, and Z. Liang, "Steerable catheters in minimally invasive vascular surgery," *Int. J. Med. Rob. Comput. Assist. Surg.* **5**(4), 381–391 (2009).
- ⁸J. Bradfield, R. Tung, R. Mandapati, N. G. Boyle, and K. Shivkumar, "Catheter ablation utilizing remote magnetic navigation: A review of applications and outcomes," *Pacing Clin. Electrophysiol.* **35**(8), 1021–1034 (2012).
- ⁹L. Flacton, Thesis, École Polytechnique Fédérale de Lausanne, Switzerland, 2013.
- ¹⁰S. Ernst, F. Ouyang, C. Linder, K. Herting, F. Stahl, J. Chun, H. Hachiya, D. Bänsch, M. Antz, and K.-H. Kuck, "Initial experience with remote catheter ablation using a novel magnetic navigation system magnetic remote catheter ablation," *Circulation* **109**(12), 1472–1475 (2004).
- ¹¹F. Carpi and C. Pappone, "Stereotaxis Niobe® magnetic navigation system for endocardial catheter ablation and gastrointestinal capsule endoscopy," *Expert Rev. Med. Devices* **6**(5), 487–498 (2009).
- ¹²B. L. Nguyen, J. L. Merino, and E. S. Gang, "Remote navigation for ablation procedures—A new step forward in the treatment of cardiac arrhythmias," *European Cardiology* **6**(3), 50–56 (2010).
- ¹³D. Filgueiras-Rama, A. Estrada, J. Shachar, S. Castrejón, D. Doiny, M. Ortega, E. Gang, and J. L. Merino, "Remote magnetic navigation for accurate, real-time catheter positioning and ablation in cardiac electrophysiology procedures," *J. Visualized Exp.* **74**, e3658 (2013).
- ¹⁴E. S. Gang, B. L. Nguyen, Y. Shachar, L. Farkas, L. Farkas, B. Marx, D. D. Johnson, M. C. Fishbein, C. Gaudio, and S. J. Kim, "Dynamically shaped magnetic fields initial animal validation of a new remote electrophysiology catheter guidance and control system," *Circ.: Arrhythmia Electrophysiol.* **4**(5), 770–777 (2011).
- ¹⁵M. P. Kummer, J. J. Abbott, B. E. Kratochvil, R. Borer, A. Sengul, and B. J. Nelson, "OctoMag: An electromagnetic system for 5-DOF wireless micromanipulation," *IEEE Trans. Rob.* **26**(6), 1006–1017 (2010).
- ¹⁶S. Erni, S. Schürle, A. Fakhraee, B. E. Kratochvil, and B. J. Nelson, "Comparison, optimization, and limitations of magnetic manipulation systems," *J. Micro-Bio Rob.* **8**(3-4), 107–120 (2013).
- ¹⁷Y. Shachar, "Apparatus and method for shaped magnetic field control for catheter, guidance, control, and imaging" (Google Patents, 2011), see <https://www.google.com/patents/US8027714>.
- ¹⁸Y. Shachar, "Apparatus and method for shaped magnetic field control for catheter, guidance, control, and imaging" (Google Patents, 2012), see <http://www.google.com/patents/US20120143127>.
- ¹⁹P. Moftakhar, P. Lillaney, A. D. Losey, D. L. Cooke, A. J. Martin, B. R. Thorne, R. L. Arenson, M. Saeed, M. W. Wilson, and S. W. Hetts, "New-generation laser-lithographed dual-axis magnetically assisted remote-controlled endovascular catheter for interventional MR imaging: *In vitro* multiplanar navigation at 1.5 T and 3 T versus x-ray fluoroscopy," *Radiology* **277**, 842–852 (2015).
- ²⁰A. D. Losey, P. Lillaney, A. J. Martin, D. L. Cooke, M. W. Wilson, B. R. Thorne, R. S. Sincic, R. L. Arenson, M. Saeed, and S. W. Hetts, "Magnetically assisted remote-controlled endovascular catheter for interventional MR imaging: *In vitro* navigation at 1.5 T versus x-ray fluoroscopy," *Radiology* **271**(3), 862–869 (2014).
- ²¹P. Lillaney, C. Caton, A. J. Martin, A. D. Losey, L. Evans, M. Saeed, D. L. Cooke, M. W. Wilson, and S. W. Hetts, "Comparing deflection measurements of a magnetically steerable catheter using optical imaging and MRI," *Med. Phys.* **41**(2), 022305 (9pp.) (2014).
- ²²P. Peichl and J. Kautzner, "Advances in irrigated tip catheter technology for treatment of cardiac arrhythmias," *Recent Pat. Cardiovasc. Drug Discovery* **8**(1), 10–16 (2013).
- ²³M. P. Armacost, J. Adair, T. Munger, R. R. Viswanathan, F. M. Creighton, D. T. Curd, and R. Sehra, "Accurate and reproducible target navigation

- with the stereotaxis Niobe® magnetic navigation system,” *J. Cardiovasc. Electrophysiol.* **18**(s1), S26–S31 (2007).
- ²⁴R. A. Serway, J. W. Jewett, K. Wilson, and A. Wilson, *Physics* (Cengage Learning Australia, South Melbourne, Vic, 2013).
- ²⁵M. N. Sadiku, *Numerical Techniques in Electromagnetics* (CRC Press, Boca Raton, FL, 2000).
- ²⁶J. Jin, *The Finite Element Method in Electromagnetics* (John Wiley & Sons, Hoboken, NJ, 2014).
- ²⁷H. Marino, C. Bergeles, and B. J. Nelson, “Robust electromagnetic control of microrobots under force and localization uncertainties,” *IEEE Trans. Autom. Sci. Eng.* **11**(1), 310–316 (2014).
- ²⁸O. Ergeneman, C. Bergeles, M. P. Kummer, J. J. Abbott, and B. J. Nelson, *Surgical Robotics* (Springer, New York, NY, 2011), pp. 271–311.
- ²⁹M. W. Spong and M. Vidyasagar, *Robot Dynamics and Control* (John Wiley & Sons, Hoboken, NJ, 2008).
- ³⁰K. W. Yung, P. B. Landecker, and D. D. Villani, “An analytic solution for the force between two magnetic dipoles,” *Magn. Electr. Sep.* **9**, 39–52 (1998).
- ³¹F. P. Gosselin, V. Lalande, and S. Martel, “Characterization of the deflections of a catheter steered using a magnetic resonance imaging system,” *Med. Phys.* **38**(9), 4994–5002 (2011).
- ³²G. Nölker, K.-J. Guteleben, B. Muntean, J. Vogt, D. Horstkotte, L. D. Abkenari, F. Akca, and T. Szili-Torok, “Novel robotic catheter manipulation system integrated with remote magnetic navigation for fully remote ablation of atrial tachyarrhythmias: A two-centre evaluation,” *Europace* **112**, 1715–1718 (2012).
- ³³S. Floyd, C. Pawashe, and M. Sitti, *presented at the IEEE International Conference on Robotics and Automation ICRA* (2008).
- ³⁴K. B. Yesin, K. Vollmers, and B. J. Nelson, “Modeling and control of untethered biomicrorobots in a fluidic environment using electromagnetic fields,” *Int. J. Rob. Res.* **25**(5-6), 527–536 (2006).
- ³⁵J. Kauphusman, H. Wang, J. Dando, and H. Puryear, “Irrigated ablation catheter having magnetic tip for magnetic field control and guidance” (Google Patents, 2008), see <http://www.google.com/patents/US20080091193>.
- ³⁶T. T. Tegg and J. V. Kauphusman, “Magnetically guided catheters” (Google Patents, 2012), see <http://www.google.com.ar/patents/US20120221001>.
- ³⁷A. de la Rama, C. Pappone, P. C. Chen, C. Hata, and J. A. Shimizu, “Magnetically guided catheter with flexible tip” (Google Patents, 2014), see <http://www.google.com/patents/US8827910>.
- ³⁸I. Tunay, “Modeling magnetic catheters in external fields,” in *The 26th Annual International Conference of the IEEE Engineering in Medicine and Biology Society* (IEEE Engineering in Medicine and Biology Society, 2004), Vol. 3, p. 2006.
- ³⁹E. J. Hearn and Ebrary, “An introduction to the mechanics of elastic and plastic deformation of solids and structural materials,” in *Mechanics of Materials* (Butterworth-Heinemann, San Diego, CA, 1997), Vol. 1.
- ⁴⁰R. P. Feynman, R. B. Leighton, and M. Sands, *Feynman Lectures on Physics, Vol. II-The New Millennium Edition: Mainly Electromagnetism and Matter* (Basic Books, New York, NY, 2011).
- ⁴¹A. Kimiaeifar, N. Tolou, A. Barari, and J. Herder, “Large deflection analysis of cantilever beam under end point and distributed loads,” *J. Chin. Inst. Eng.* **37**(4), 438–445 (2014).
- ⁴²T. Beléndez, C. Neipp, and A. Beléndez, “Large and small deflections of a cantilever beam,” *Eur. J. Phys.* **23**(3), 371–379 (2002).
- ⁴³A. Banerjee, B. Bhattacharya, and A. Mallik, “Large deflection of cantilever beams with geometric non-linearity: Analytical and numerical approaches,” *Int. J. Non-Linear Mech.* **43**(5), 366–376 (2008).
- ⁴⁴T. Wang, S. Lee, and O. Zienkiewicz, “A numerical analysis of large deflections of beams,” *Int. J. Mech. Sci.* **3**(3), 219–228 (1961).
- ⁴⁵J. Kierzenka and L. F. Shampine, “A BVP solver based on residual control and the Matlab PSE,” *ACM Trans. Math. Software* **27**(3), 299–316 (2001).
- ⁴⁶L. Shampine, “Solving a hard BVP with bvp4c” (private communication, 2004).
- ⁴⁷L. F. Shampine, J. Kierzenka, and M. W. Reichelt, “Solving boundary value problems for ordinary differential equations in MATLAB with bvp4c,” Tutorial Notes, 2000.
- ⁴⁸I. S. Grant and W. R. Phillips, *Electromagnetism* (Wiley, Hoboken, NJ, 2013).
- ⁴⁹T. H. Boyer, “The force on a magnetic dipole,” *Am. J. Phys.* **56**(8), 688–692 (1988).